Polarization-controllably launching localized cosine-Gauss beam with spatially varied metallic nano-apertures

Xuesi Zhao, Xue Feng,[*] Peng Zhao, Fang Liu, Kaiyu Cui, Wei Zhang, and Yidong Huang

Department of Electronic Engineering, Tsinghua University, Beijing, China
*x-feng@tsinghua.edu.cn

Abstract: Two properly designed columns of orthogonally tilted and spatially varied nano-apertures have been demonstrated to achieve polarization-controlled launching of the localized cosine-Gauss beam, which is a kind of highly localized surface plasmonic wave without diffraction. According to the experimental results, the generated unidirectional propagating plasmonic beam could propagate with a non-diffracting length of up to 57μm as well as the extinction ratio of more than 150. We believe that our proposed device would play an important role in highly compact photonic circuit on-chip with plasmonic wave.

1. Introduction

Surface plasmon polariton (SPP) wave has attracted more and more attentions due to field confinement within subwavelength scale [1–3]. Hence, it has been applied in various fields ranging from sensing [4], nonlinear enhancement [5,6], to particle manipulation [7–9], *etc.* Furthermore, it would be greatly helpful to achieve highly compact on-chip circuit with SPP wave [10–14]. To achieve it, both controlling excitation and propagation of SPP wave are essential. To excite the SPP wave, several structures such as gratings [15], single slit [16] or prism-based scheme [17] have been proposed and demonstrated. However, there are two limitations. The first one is that only the perpendicular polarization component (according to the coupling structure) of incident optical wave can be coupled to plasmonic waves due to the transverse magnetic (TM) nature. It means the cross-polarized component cannot be utilized. The other is that the poor coupling directionality would lead to lower efficiency and introduce additional noise [18]. To address the aforementioned limitations, Lin et al. have presented a directional SPP coupler with polarization-invariant coupling efficiency [18], in which two columns of uniform nano-apertures on the metal film are employed. For each column, a polarization-dependent phase term is introduced to the generated SPP wave. Thus, by controlling the polarization state of incidence, the energy ratio between the two propagating SPP waves in both sides could be controllably varied. However, although the excitation has been well addressed in [18], the generated SPP wave would still suffer from the wave diffraction. Obviously, it would be hard to manipulate and detect a diverged SPP wave. To reduce the diffraction, there are several works about non-diffracting SPP beam that have been proposed, such as Bessel-like beams [19–28], Airy beam [29–33], bottle beams [34,35] and arbitrary bending plasmonic beams [36], *etc*. Among them, the localized cosine-Gauss beam (LCGB) [19–22,27,28] is a kind of Bessel-like beam and originates from the interference of two tilted SPP beams. It should be noticed that the LCGB would propagate along a straight line while the intensity of the beam keeps in the main lobe. Thus, it is very promising for transmission, manipulation and detection. Based on the directional SPP coupler demonstrated in [18], if the apertures could be properly designed to generate LCGB, polarization-controlled directional launching of non-diffracting SPP waves could be achieved. Actually, it is the motivation of this work.

In this work, a modified SPP coupler is designed and fabricated to achieve polarization-controlled directional launching of the LCGB. As reported in the previous work [20,21], the key point to generate LCGB is how to introduce a spatially distributed phase gradient on the generated SPP wave. In [18], all nano-apertures have uniform geometrical shape so that there is no phase gradient and as a result, the generated SPP wave would diverge. Hence, the most direct way is properly modulating the nano-apertures to achieve the required phase gradient. There are several works to modulate the wavefront of SPP beams through modulating the geometric dimension [33,37], orientation [19,32,38–40] or longitudinal position [18,20,22,25,41,42] of each nano-aperture. However, according to our analysis, the only option is to modulate the geometric dimensions of each nano-aperture to achieve the maximum extinction ratio and coupling efficiency, which would be discussed in Sec.2. Thus, in our proposal, two columns of nano-apertures on gold film are aligned together while the geometric dimensions of the nano-apertures in each column have been properly arranged to obtain a spatially distributed phase gradient to launch the LCGB. By controlling the polarization state of incidence, the energy ratio between the two propagating LCGBs in both sides can be controlled. Additionally, the propagation characteristics of generated LCGB have also been investigated with two different kinds of couplers.

2. Principle

The proposed structure is etched on a metal film and consists of two columns of orthogonally tilted and spatially varied nano-apertures as shown in Fig. 1(a). Each column could generate LCGB in both sides by introducing a phase modulation while polarization controlled directional launching could be achieved by both two columns [18]. To present the principle more clearly, one column of the nano-apertures would be discussed at first.

To generate the SPP wave propagating along the metal film, a series of tilted nano-apertures can be aligned into one column along the y-axis with a subwavelength period d as shown in Fig. 1(b), where $m = -N \sim N$ indicates the mth aperture located in the position of $(0, md)$. When these apertures are illuminated by an incident light with angle frequency of ω, the excited SPP wave can be written as [43]:

$$\vec{E}_\pm(\vec{r}, t) = \sum_{m=-N}^{N} A_m \exp(\mathrm{i}\varphi_m) \exp(-\mathrm{i}\omega t) \frac{\cos(\theta_m' - \theta_m)}{\sqrt{|\vec{r} - \vec{r_m}|}} \exp(\mathrm{i}k_{\mathrm{SPP}} |\vec{r} - \vec{r_m}|) e^{-k_z z} \hat{a}_\pm, \quad (1)$$

where the sign of ($\pm$) corresponds to the SPP wave propagating in the positive /negative x-direction. A_m and φ_m are the amplitude and phase of the excited field by the mth aperture respectively. $\vec{r_m}$ and θ_m are the position and tilt angle of the mth aperture, $\vec{r}$ is the space displacement vector, θ_m' is the off-angle between the vector of $\vec{r}$ and $\vec{r} - \vec{r_m}$, k_{SPP} and k_z are the propagation constant and evanescent wave decay coefficient of SPP wave, respectively. $\hat{a}$ is the unit vector and given by $\hat{a}_\pm = -\left(|k_z|^2 + |k_{\mathrm{SPP}}|^2\right)^{-\frac{1}{2}} (-\mathrm{i}k_z, 0, \pm k_{\mathrm{SPP}})$.

The excited SPP wave can be modulated by properly controlling all of the nano-apertures. For simplicity, the tilt angle of each aperture is assumed as identical ($\theta_m = \theta, m = -N \sim N$).

2.1 Plane SPP Wave

When one column is designed with the amplitude and phase distribution of $A_m = A \exp\left[-(md)^2 / W_0^2\right]$ (W_0 is the beam waist of incident light wave) and $\varphi_m = \varphi, m = -N \sim N$, respectively, the excited SPP wave can be expressed as:

$$\vec{E}_\pm(x,y,z,t) = A\sin(\theta)\sqrt{\frac{\mathrm{i}2\pi}{k_{\mathrm{SPP}}}}\exp\left(\frac{-y^2}{W_0^2}\right)\exp\left[\mathrm{i}(k_{\mathrm{SPP}}x+\varphi)\right]\exp(-\mathrm{i}\omega t - k_z z)\hat{a}_\pm. \quad (2)$$

More details are shown in the Appendix and the corresponding wavefront distribution is shown in Fig. 1(c). Obviously, it is a plane wave.

2.2 Localized cosine-Gauss beam (LCGB)

The LCGB is a kind of SPP wave without diffraction and the propagation distance can be more than several dozens of SPP wavelength. LCGB can be generated by two intersecting plane SPP beams with a rotational angle α and the electric field can be expressed as [20]:

$$E_z(x,y) \propto \exp\left(\frac{-y^2}{W_0^2}\right)\cos\left[k_{\mathrm{SPP}}y\sin(\alpha)\right]. \quad (3)$$

The wavefront of such beam would be "Λ"-shaped with the opening angle of $(180-2\alpha)°$. When one column is designed with the amplitude (phase) distribution of $A_m = A\exp\left[-(md)^2/W_0^2\right]$ $\left(\varphi_m = -k_{\mathrm{SPP}}|md|\sin(\alpha), m = -N \sim N\right)$, the excited SPP waves can be expressed as:

$$\vec{E}_\pm(x,y,z,t) = A\sin(\theta)F(x)\exp\left(\frac{-y^2}{W_0^2}\right)\cos\left[k_{\mathrm{SPP}}y\sin(\alpha)\right]\exp(\mathrm{i}k_{\mathrm{SPP}}x)\exp(-\mathrm{i}\omega t - k_z z)\hat{a}_\pm.$$

$$(4)$$

Here $F(x)$ is a function dependent on α and the expression can be found in Appendix. Actually, the generated SPP wave is LCGB and the corresponding wavefront distribution with $\alpha = 3°$ and $\alpha = 5°$ are shown in Figs. 1(d) and 1(e), respectively. Besides, if the incident light is not normal to the interface but with an angle of β according to y-axis, additional phase distribution of $\varphi(y) = k_{\mathrm{SPP}}y\sin(\beta)$ would be introduced so that the inclined-LCGB with angle of β would be generated accordingly [21,22,34] (The detailed analysis and discussions are shown in Appendix).
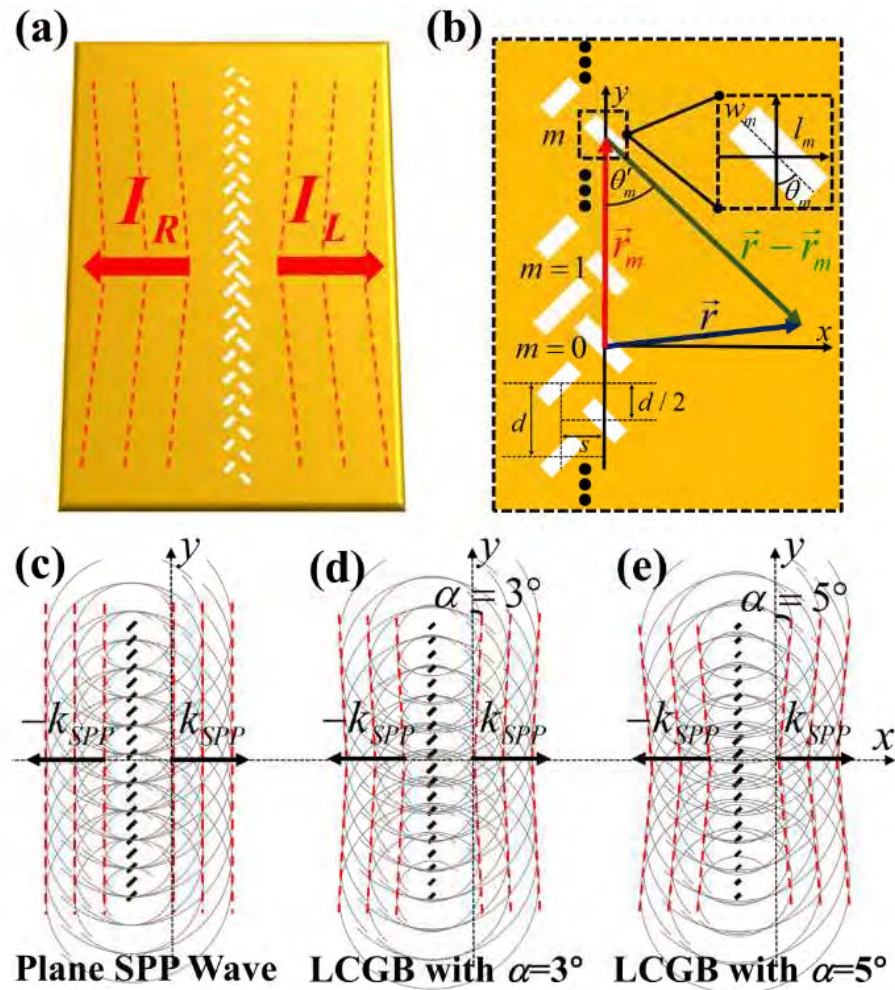
Fig. 1. (a) Schematic of the proposed SPP coupler for polarization-controlled directional launching of LCGB, which consists of two columns of spatially varied nano-apertures. The red dashed line shows the wavefront distribution of generated LCGB and the red arrows show the propagation directions for LHCP and RHCP, respectively. (b) Top views of one column of nano-apertures with the parameters and corresponding coordinate. (c-e) The wavefront of plane SPP wave, LCGB with $\alpha = 3°$ and $\alpha = 5°$, respectively (from left to right). The red dashed lines denote the shape of the wavefront and the black arrows are the propagation directions of the generated surface waves.

It should be noticed that in both cases mentioned above, the SPP waves propagating in both sides can only be excited along a fixed direction in spite of the tilt angle of nano-aperture. However, both the amplitude and phase of the excited SPP wave strongly depend on the tilt angle. Thus, interference between two adjacent columns of nano-apertures with different tilt angles can be applied to control the propagation direction of generated SPP wave as demonstrated in [18]. Similarly, two adjacent columns with spatially varied nano-apertures as shown in Fig. 1(a) can be designed to achieve the polarization-controlled directional launching of LCGB. Here, the distance of two parallel columns is denoted as s while the spacing between two adjacent apertures is set as d in each column with $d < \lambda_{\text{SPP}}$ (λ_{SPP} is the wavelength of exited SPP wave). Besides, there is an offset distance of $d/2$ along y-axis to reduce scattering due to adjacent apertures in two columns [18].

When a circularly polarized plane wave is incident on a pair of adjacent nano-apertures in two columns, the time-averaged intensities of generated SPP wave in both sides can be expressed as:

$$I_{\pm} \propto \left|\vec{E_1}\right|^2 \sin^2(\theta_1) + \left|\vec{E_2}\right|^2 \sin^2(\theta_2) + 2\left|\vec{E_1}\right|\left|\vec{E_2}\right|\sin(\theta_1)\sin(\theta_2)\cos\left[(\varphi_2-\varphi_1)\mp k_{SPP}s\right], \quad (5)$$

where the subscript of i ($i = 1,2$) indicates the corresponding nano-aperture in the left or right column, $\left|\vec{E_i}\right|$ is the amplitude, θ_i is the tilt angle of nano-aperture according to the y-axis, φ_i is the initial phase of the excited SPP wave, the sign of ($\pm$) corresponds to the SPP propagating along the positive or negative x-direction, respectively. After some deductions (details shown in Appendix), the maximum extinction conditions can be obtained:

$$k_{SPP}s = \frac{\pi}{2}; \theta_1 = \frac{\pi}{4}; \theta_2 = \frac{3\pi}{4}. \quad (6)$$

With such conditions, the time-averaged intensities of SPP wave in both sides can be further expressed as:

$$I_+ \propto 2 + 2\cos\left[\pm(\theta_2-\theta_1)+\frac{\pi}{2}\right]; I_- \propto 2 + 2\cos\left[\pm(\theta_2-\theta_1)-\frac{\pi}{2}\right], \quad (7)$$

where the sign of ($\pm$) in the phase term $\pm(\theta_2-\theta_1)$ corresponds to incidence with right-handed circular polarization (RHCP)/the left-handed circular polarization (LHCP). Equation (7) indicates that the SPP could only propagate towards the positive/ negative x-axis for the incidence with LHCP/RHCP.

To obtain the required phase gradient for launching LCGB, the apertures have to be modulated. However, to achieve the maximum extinction ratio and coupling efficiency, the tilt angle of each nano-aperture has to be fixed at 45° according to Eq. (6). Thus, the only option is to modulate the geometric dimensions of each nano-aperture.

3. Simulation results

To find out the field responses of nano-apertures with tilt angle of 45°, the finite-different time-domain (FDTD) simulations have been performed with sweeping width ($w = 0 \sim 120\,\text{nm}$) and length ($l = 200 \sim 400\,\text{nm}$). The thickness of gold film and the operation wavelength are set as 100nm and $\lambda = 980\text{nm}$ (corresponding to $\lambda_{SPP} \approx 960\text{nm}$), respectively. To calculate the performance of our proposed device, the periodic boundary condition (PBC) is employed along y-direction and the period of such structure is set as $d = 480\,\text{nm}$ (half of λ_{SPP}).

Both the calculated amplitude and phase responses are shown in Figs. 2(b)-2(c), respectively, while the amplitude is normalized by the maximum amplitude of all calculated results. It can be found that both the amplitude (A) and phase (φ) strongly depend on the width and length. Thus, it is very convenient and flexible to obtain the desired phase distribution of $\varphi(y) = -k_{SPP}|y|\sin(\alpha)$. To demonstrate it, two cases of $\alpha = 3°$ and $\alpha = 5°$ are considered. For each case, there are five kinds of apertures and the phase gradient is 0.34rad/μm (0.55rad/μm) for $\alpha = 3°$ ($\alpha = 5°$), respectively. The corresponding geometric parameters and field response are shown in Figs. 2(d)-2(e), respectively.
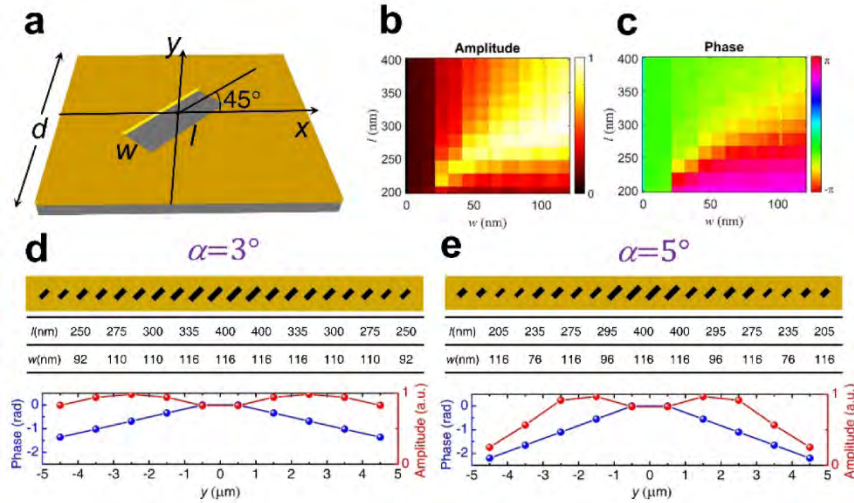
Fig. 2. (a) Schematic of one 45° tilted rectangular nano-aperture with length of l and width of w etched on the gold film. (b) and (c) are the calculated amplitude and phase responses versus length of l and width of w, respectively. The amplitude is normalized by the maximum amplitude of all calculated results. (d) and (e) The corresponding geometric parameters and field response for five kinds of apertures to obtain the required phase distribution for $\alpha = 3°/\alpha = 5°$.

To achieve polarization-controlled launching of LCGB, the distance between two columns of nano-apertures is set as $s = 240$nm according to the Eq. (6). The results obtained by FDTD simulations are summarized in Fig. 3. As shown in Figs. 3(a)-3(b), the generated LCGBs can only propagate towards the positive/ negative x-axis for the incidence with LHCP/RHCP for both cases of $\alpha = 3°$ and $\alpha = 5°$. Thus the polarization-controlled directional launching of LCGB have been achieved. Besides, the calculated electric field distributions of normal component in both cases are shown in Figs. 3(c)-3(d). For both cases, there are two processes along the x-axis. The first one is the formation of LCGB, in which the excited SPP wave converges to a spot. The minimum transverse size of the spot is the beam waist of generated LCGB and denoted as ω_0.

After that, the second process is that LCGB propagates with a beam divergence angle of θ_{div}, which is related to the diffracting condition of a paraxial beam. As shown in Eq. (4), the propagation characteristics of generated LCGBs would strongly depend on the rotational angle of α. From Figs. 3(c)-3(d), it can be found that the "Λ"-shaped wavefront of LCGB with $\alpha = 3°$ has a larger opening angle than that with $\alpha = 5°$. For more clarity, the relation between beam width of the generated LCGB and the longitudinal position is depicted in Figs. 3(e)-3(f) for $\alpha = 3°$ and $\alpha = 5°$, respectively. Furthermore, both the beam waist of ω_0 and divergence angle of θ_{div} can be obtained. For $\alpha = 3°$, there is a smaller divergence angle (0.064rad vs. 0.091rad) but a larger beam waist (1.96μm vs.1.70μm) than that with $\alpha = 5°$. Moreover, we define the non-diffracting length L_{eff} of LCGB as the longest distance while the beam width is smaller than half size of the coupler (about 4.5μm). When the beam width is larger than that size, energy carried by surface beam cannot be confined in the core area of the device, thus leading to undesirable crosstalk. It should be noted that the non-diffracting length is shorter than the standard SPP propagation length and the related discussion is given in the Appendix.

According to the results shown in Figs. 3(e)-3(f), the non-diffracting length is $L_{eff} = 58$μm$/L_{eff} = 50$μm with $\alpha = 3°/\alpha = 5°$. These results indicate that the propagation characteristics of generated LCGB can be controlled by properly setting the value of α [20,21,24,28]. Similar to that shown in [20], the non-diffracting length of LCGB can be longer by increasing the number of the nano-apertures within one column. However, it would increase

the footprint of the device. Thus, there is a tradeoff between the compactness of device and the propagation length of LCGB, which should be properly balanced according to the specific applications.
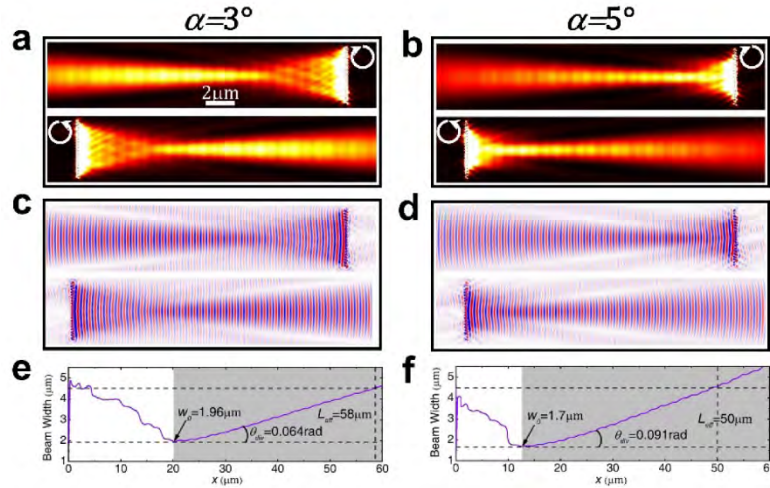
Fig. 3. (a) The FDTD simulation results of polarization-controlled directional launching of LCGB with $\alpha = 3°$ and $\alpha = 5°$, respectively. (a) and (b) are the intensity distributions of polarization-controlled unidirectional LCGB for the incidence with RHCP and LHCP, respectively. (c) and (d) are the electric field distributions of normal component. (e) and (f) are the relation between beam width of the generated LCGB and the longitudinal position and the parameters (beam waist, divergence angle, non-diffracting length) for describing propagation characteristics are also given.

4. Experimental results

To verify our proposal, several samples have been fabricated by a focused ion beam machine (FIB) (Tescan LYRA3). A 100nm thick gold thin film is evaporated on the quartz substrate with a 5nm thick buffer layer of titanium through vapor deposition. Figure 4(a) is the scanning electron microscope (SEM) image of the whole structure composed of LCGB couplers with $\alpha = 3°$ and the enlarged area shows the details. There are five couplers aligned together with a period of one SPP wavelength (~960nm) to achieve higher coupling efficiency. According to the FDTD simulation, the coupling efficiency is ~3.5%, which is consistent to the value of ~3.2% given in [18]. It should be mentioned that the efficiency could be further improved by increasing the number of couplers or adopting low-loss plasmonic materials. Besides, there are two annular gratings in both sides to scatter the generated LCGB into propagation mode in free-space for measurement and the spacing between the two gratings is about 65μm. The coupler with $\alpha = 5°$ is also fabricated and shown in Appendix. For the measurement, a 980nm laser source (Thorlabs, CLD1015) is incident onto the sample followed by a polarizer and a quarter wave plate (QWP), then focused by an objective (Nikon, NA = 0.3), and the other objective (Nikon, NA = 0.3) is used for collecting the scattering light by the annular gratings. The optical signal scattered by gratings is detected by a charge-coupled device (CCD) camera (Thorlabs, 4070M-USB).
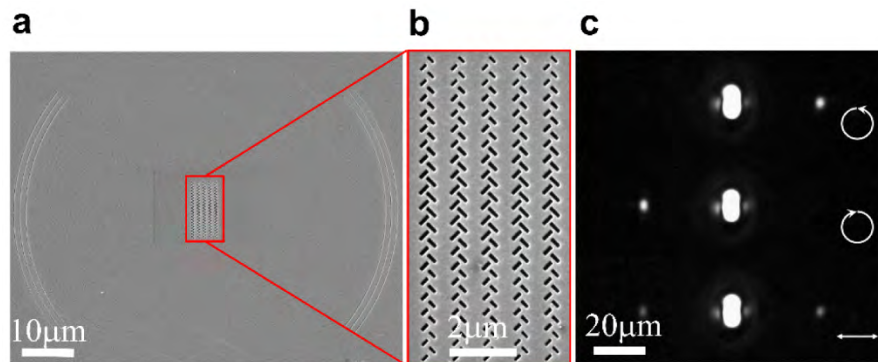
Fig. 4. (a) The SEM image of the whole structure and the annular gratings in both sides to scatter the generated LCGB into propagation mode in free-space for measurement. (b). The enlarged area is the couplers group composed of five couplers with $\alpha = 3°$. (c) The measured signals of polarization-controlled directional propagation of generated LCGB with LHCP, RHCP and LP, respectively. A short video about it is provided in Visualization 1.

The intensity of optical signals scattered by the two annular gratings depends on the state of polarization (SOP) of incidence. A short video about it is provided in Visualization 1. The typical results for incidence with RHCP, LHCP and linear polarization (LP) are shown in Fig. 4(c). With LHCP incidence, the optical signals can only be observed in the right side and vice versa with LP incidence, the optical signals are in both sides. Therefore, it can be concluded that the propagation direction of LCGB is well controlled by the SOP of incident light. Furthermore, the extinction ratio of the coupler has been estimated. According to the calculated results, the optical waists in both sides are nearly the same as well as nearly at the same position. Thus, the SPP wave generated in both sides can be considered as the same Gaussian intensity distribution so that the extinction ratio could be approximately calculated as the ratio of peak intensity. The measured extinction ratio is ~150, ~160 and ~1.1 for incidence with RHCP, LHCP and LP, respectively. There is a little difference of the extinction ratio between the RHCP and LHCP, which may be due to the error from fabrication, measurement and alignment.
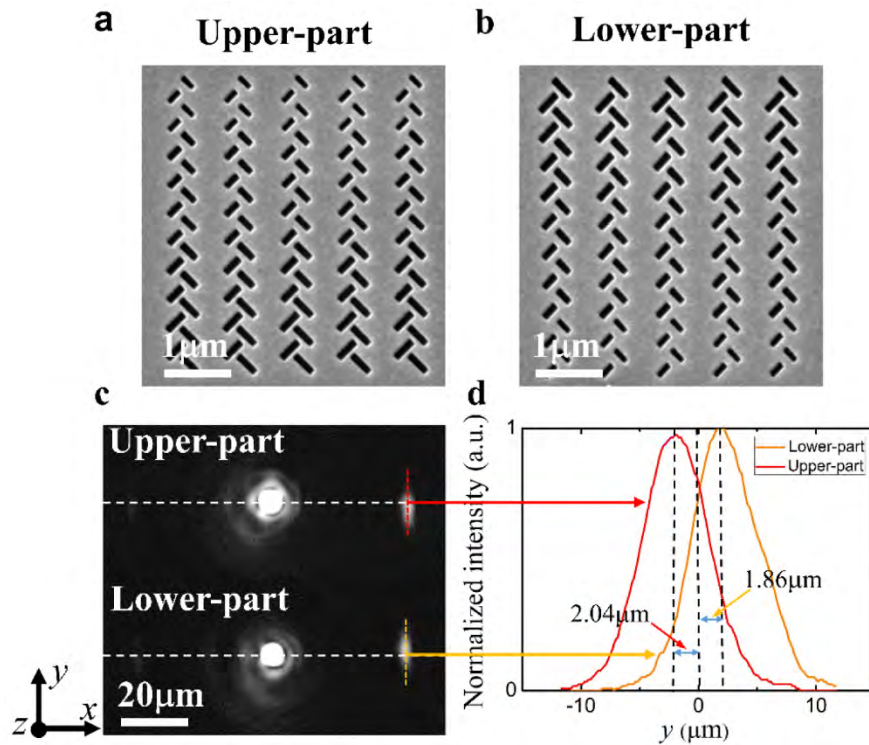
Fig. 5. (a-b) The SEM image of upper-part and lower-part with $\alpha = 3°$. (c) The measured signals of upper-part and lower-part for incidence with LHCP. (d) The normalized intensity distribution along y-axis of scattered spot.

It should be noted that the LCGB originates from the interference of two opposite tilted SPP beam and thus possesses the phase distribution of $\varphi(y) = -k_{\mathrm{SPP}}|y|\sin(\alpha)$. Therefore, to verify the induced phase distribution, we have fabricated and measured samples with only upper-part ($y>0$) and lower-part ($y<0$) of our proposed structure as shown in Figs. 5(a)-5(b), respectively. Theoretically, upper-part would induce the negative linear phase gradient along y-axis of $k_- = -k_{\mathrm{SPP}}\sin(\alpha)$ while lower-part would induce positive phase gradient of $k_+ = k_{\mathrm{SPP}}\sin(\alpha)$.

Due to the linear phase gradient, the generated SPP beam of upper-part (lower-part) would tilt toward negative (positive) y-axis with a tilt angle of α as discussed in Sec. 2. Figure 5(c) shows the collected light scattered by gratings in 40μm away with upper-part and lower-part, respectively. It can be found that the scattered spot exists in negative (positive) y-axis for upper-part (lower-part), which is consistent with above discussions. Furthermore, the intensity distribution of scattered spot is also shown in Fig. 5(d). The separation distance is about −2.04μm (1.86μm) corresponding to a tilt angle of 2.92° (2.67°), which is very close to the preset angle of $\alpha = 3°$. These results could confirm that the upper-part and lower-part have successfully generated opposite tilted SPP beams, which is desired to generate the LCGB.
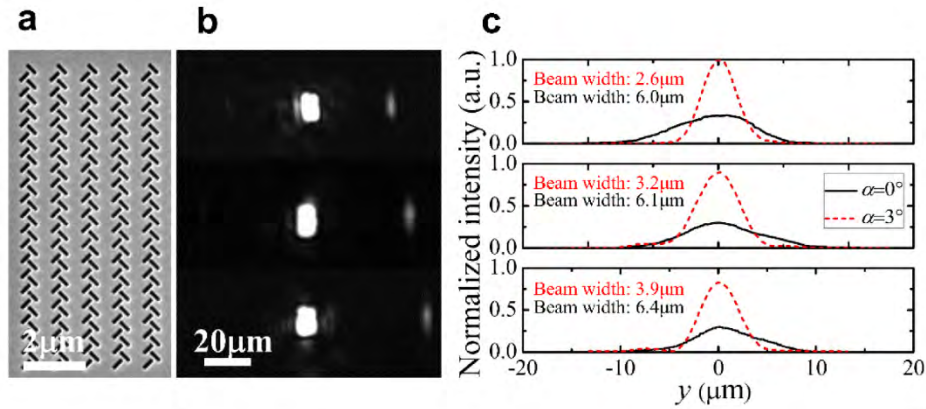
Fig. 6. The SEM image of SPP coupler with $\alpha = 0°$. (b) The experimental results for incidence with LHCP in different longitudinal positions (30μm, 40μm, 50μm). (c) The normalized intensity distribution of scattered spot for SPP coupler with $\alpha = 0°$ (black solid line) and $\alpha = 3°$ (red short dash line) in different longitudinal positions (30μm, 40μm, 50μm) and the beam width is also given.

Additionally, a SPP coupler with $\alpha = 0°$ as shown in Fig. 6(a) is also fabricated for comparison. In this case, several pairs of orthogonally tilted nano-apertures with the same shape ($w = 120\,\text{nm}$ and $l = 400\,\text{nm}$). Figure 6(b) shows the scattering light collected by the CCD camera with incidence of LHCP in different longitudinal positions (30μm, 40μm, 50μm). Figure 6(c) shows comparison between the beam intensity distribution of $\alpha = 0°$ and $\alpha = 3°$ in different longitudinal positions (30μm, 40μm, 50μm), which is normalized by the maximum intensity of $\alpha = 3°$ in position of 30μm. It could be found that the energy of $\alpha = 3°$ is more concentrated than that of $\alpha = 0°$. Furthermore, by Gaussian fitting, the $1/e^2$ beam width can be obtained and marked in Fig. 6 (c). The beam width of $\alpha = 0°$ is 6.0μm/6.1μm/6.4μm at position of 30μm/40μm/50μm, which is distinctly larger than case of $\alpha = 3°$ (2.6μm/3.2μm/3.9μm). Therefore, the SPP beam generated by our proposed structure would possess a smaller beam width, which is consistent to the propagation characteristics of LCGB mentioned in Sec.3.

Through the verification of phase distribution and the comparison with a uniform SPP coupler, it could be indirectly confirmed that the LCGB has been generated.
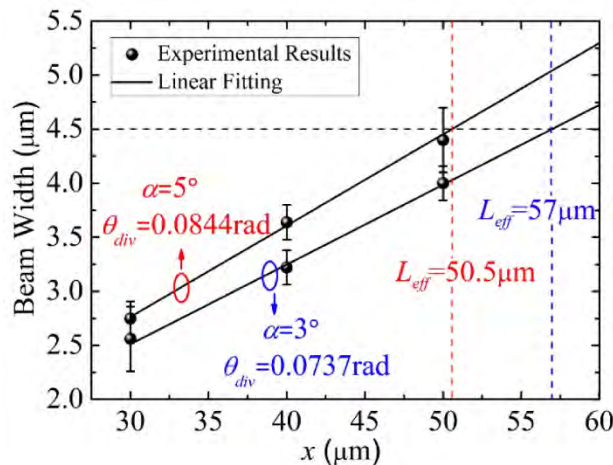
Fig. 7. The relation between beam width of the generated LCGBs and the longitudinal position for $\alpha = 3°$ and $\alpha = 5°$. The divergence angles and non-diffracting length of both cases are also given.

To measure the propagation characteristics of the generated LCGB, the annular gratings have been etched at different positions along the propagation direction. Figure 7 shows the experimental results of the relation between the beam width and the longitudinal position for both cases of $\alpha = 3°$ and $\alpha = 5°$, respectively. By linear fitting, the propagation characteristics of generated LCGBs in both cases can be obtained. For the LCGB with $\alpha = 3°$, the divergence angle is smaller (0.0737rad vs.0.0844rad) and the non-diffracting length is larger (57μm vs.50.5μm) than that with $\alpha = 5°$ accroding to the experimental results. The relative fitting errors of the beam divergence angle with experimental results are ~20% and 18% for cases of $\alpha = 3°$ and $\alpha = 5°$, respectively. Comparing with the simulation results of 0.064rad ($\alpha = 3°$) and 0.091rad ($\alpha = 5°$), there is only a little difference between the experimental and simulated results. It is mainly caused by the fabrication error and could be improved by more accurate fabrication process. It should be mentioned that the divergence angle of LCGB with $\alpha = 5°$ in the experimental result is smaller than that in the simulation result. It is probably because the phase gradient obtained with the fabricated sample is smaller than the designed value.

5. Conclusions

In conclusion, we have proposed and demonstrated a modified SPP coupler to achieve polarization-controlled directional launching of the LCGB. The coupler consists of two columns of orthogonally tilted and spatially varied nano-apertures with properly designed phase distribution. The generated LCGB can propagate as long as 57μm while the beam width is smaller than half size of the coupler. Thus, the energy of SPP wave could be mainly confined in the core area of the coupler and transmitted dozens of wavelengths. Therefore, the cross-talk and propagation loss induced by the beam diffraction could be reduced compared with the plane SPP wave. It should be noted that the propagation distance can be further increased by increasing the number of the nano-apertures within one column. However, there is a tradeoff between the non-diffracting length and the footprint of device. Meanwhile, the propagation direction of generated LCGBs can be controlled by the SOP of incident light and the extinction ratio is more than 150 at operating wavelength of 980nm. Due to the polarization controllability and LCGB generation, our proposal is very promising to serve as a high-efficiency polarization beam splitter or polarization encoder and greatly potential to integrate with other devices such as modulators and detectors for the compact photonic integrated circuit.
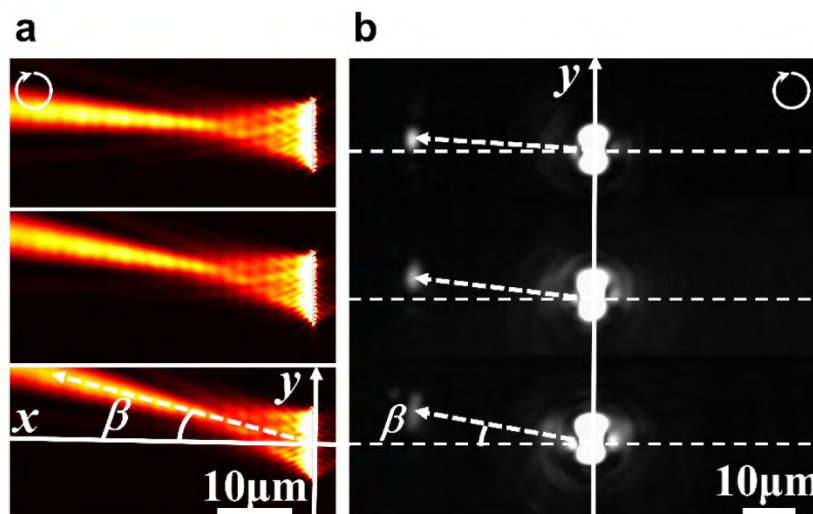
Fig. 8. (a) The simulation results of polarization-controlled directional inclined-LCGB generation with inclined angle of 5°, 10°and 15°, respectively. And the used parameters and corresponding coordinate are also given. (b) The experimental results for inclined angle of 2°, 5°and 9°, respectively.

Additionally, if the polarization-controlled LCGB coupler is illuminated by the incident light with incidence angle of β according to y-axis, the inclined-LCGB would be generated [21,22,31]. Figure 8(a) shows the simulation results with inclined angles of 5°, 10°and 15, respectively, with LHCP incidence. The experimental results with inclined angles of 2°, 5°and 9°are shown in Fig. 8(b). The propagation direction can be changed accordingly by controlling the incidence angle. Thus, multichannel coupling could be achieved with the inclined incidence and more flexibility could be obtained. Anyway, such modified SPP coupler could play an important role in highly compact photonic circuit on-chip.

Appendix

Plane SPP wave generation

When an incident light with angle frequency of ω is illuminated on those nano-apertures, the excited SPP wave can be written as [43],

$$\vec{E}_\pm\left(\vec{r},t\right) = \sum_{m=-N}^{N} A_m \exp\left(i\varphi_m\right)\exp\left(-i\omega t\right)\frac{\cos\left(\theta_m{}' - \theta_m\right)}{\sqrt{\left|\vec{r}-\vec{r_m}\right|}}\exp\left(ik_{\mathrm{SPP}}\left|\vec{r}-\vec{r_m}\right|\right)e^{-k_z z}\hat{a}_\pm, \quad (8)$$

where the sign of ($\pm$) corresponds to the SPP wave propagating in the positive /negative x-direction. A_m and φ_m are the amplitude and phase of the excited field by the mth aperture respectively. $\vec{r_m}$ and θ_m are the position and tilt angle of the mth aperture, $\vec{r}$ is the space displacement vector, $\theta_m{}'$ is the off-angle between the vector of $\vec{r}$ and $\vec{r}-\vec{r_m}$, k_{SPP} and k_z are the propagation constant and evanescent wave decay coefficient of SPP wave, respectively. $\hat{a}$ is the unit vector and given by $\hat{a}_\pm = -\left(\left|k_z\right|^2 + \left|k_{\mathrm{SPP}}\right|^2\right)^{-\frac{1}{2}}\left(-ik_z, 0, \pm k_{\mathrm{SPP}}\right)$.

When the amplitude and phase distribution are $A_m = A\exp\left[-\left(md\right)^2/W_0^2\right]$ (W_0 is the beam waist of incidence) and $\varphi_m = \varphi, m = -N \sim N$, respectively, the excited SPP wave can be written as:

$$\vec{E}_\pm\left(\vec{r},t\right) = A\exp\left[\frac{-\left(md\right)^2}{W_0^2}\right]\exp\left(i\varphi\right)\exp\left(-i\omega t\right)e^{-k_z z}\sum_{m=-N}^{N}\frac{\cos\left(\theta_m{}' - \theta_m\right)}{\sqrt{\vec{r}-\vec{r_m}}}\exp\left(ik_{\mathrm{SPP}}\left|\vec{r}-\vec{r_m}\right|\right)\hat{a}_\pm,$$

$$(9)$$

where $\theta_m{}' = \arccos\left[\dfrac{\left(\vec{r}-\vec{r_m}\right)\cdot\hat{y}_-}{\left|\vec{r}-\vec{r_m}\right|}\right]$ is the off-angle between the vector of $\vec{r}$ and $\vec{r}-\vec{r_m}$.

Then the summation of all SPP waves expressed as Eq. (9) can be approximately transferred into the definite integral shown below because the period d is small compared with the position vector of $\vec{r}$.

$$\vec{E}_\pm\left(x,y,z,t\right) = \int_{-Nd}^{Nd} A\exp\left(\frac{-y'^2}{W_0^2}\right)\frac{\cos\left\{\arccos\left[\dfrac{y'-y}{\sqrt{x^2+\left(y'-y\right)^2}}\right]-\left[\dfrac{\pi}{2}-\theta\left(y'\right)\right]\right\}}{\sqrt{\sqrt{x^2+\left(y'-y\right)^2}}}\cdots (10)$$

$$\cdots\exp\left(ik_{\mathrm{SPP}}\sqrt{x^2+\left(y'-y\right)^2}\right)\exp\left(i\varphi\right)dy'\exp\left(-i\omega t - k_z z\right)\hat{a}_\pm.$$

According the paraxial approximation, the following condition can be satisfied.

$$\sqrt{x^2 + (y' - y)^2} \gg x + (y' - y)^2 / 2x. \tag{11}$$

Besides, the integral limit can be extended to infinity when the Gaussian-modulation of amplitude is taken. For sake of simplicity, all nano-slits is assumed with the same tilt angle. Thus, the SPP field can be expressed as:

$$\vec{E}_\pm(x, y, z, t) = \int_{-\infty}^{\infty} \exp\left(ik_{SPP}\frac{y'^2 - 2yy'}{2x}\right)\exp\left(\frac{-y'^2}{W_0^2}\right)dy' A\sin(\theta)\exp(i\varphi)\cdots$$
$$\cdots\exp\left(ik_{SPP}\frac{y^2}{2x}\right)\frac{\exp(ik_{SPP}x)}{\sqrt{x}}\exp(-i\omega t - k_z z)\hat{a}_\pm. \tag{12}$$

After solving the above infinity integral [20], the SPP wave can be obtained as:

$$\vec{E}_\pm(x, y, z, t) = A\sin(\theta)\sqrt{\frac{i2\pi}{k_{SPP}}}\exp\left(\frac{-y^2}{W_0^2}\right)\exp\left[i(k_{SPP}x + \varphi)\right]\cdots$$
$$\cdots\exp(-i\omega t - k_z z)\hat{a}_\pm. \tag{13}$$

Obviously, it is a plane wave.

LCGB generation

When the amplitude and phase distribution are $A_m = A\exp\left[-(md)^2 / W_0^2\right]$ and $\varphi_m = -k_{SPP}|md|\sin(\alpha)$, $m=-N\sim N$, respectively, the excited SPP waves can be obtained as:

$$\vec{E}_\pm(\vec{r}, t) = \sum_{m=-N}^{N} A\exp\left[-(md)^2 / W_0^2\right]\exp\left[-ik_{SPP}|md|\sin(\alpha)\right]\cdots$$
$$\cdots\frac{\cos(\theta_m' - \theta_m)}{\sqrt{\vec{r} - \vec{r}_m}}\exp\left(ik_{SPP}|\vec{r} - \vec{r}_m|\right)\exp(-i\omega t - k_z z)\hat{a}_\pm. \tag{14}$$

Under the paraxial approximation and similar process as the above section, the SPP field can be expressed as:

$$\vec{E}_\pm(x, y, z, t) = \int_{-\infty}^{\infty} \exp\left(ik_{SPP}\frac{y'^2 - 2yy'}{2x}\right)\exp\left[-ik_{SPP}|y'|\sin(\alpha)\right]\exp\left(\frac{-y'^2}{W_0^2}\right)dy'\cdots$$
$$\cdots A\sin(\theta)\exp\left(ik_{SPP}\frac{y^2}{2x}\right)\frac{\exp(ik_{SPP}x)}{\sqrt{x}}\exp(-i\omega t - k_z z)\hat{a}_\pm. \tag{15}$$

After solving the above infinity integral [20], the LCGB can be obtained as:

$$\vec{E}_\pm(x, y, z, t) = A\sin(\theta)F(x)\exp(\frac{-y^2}{W_0^2})\cos\left[k_{SPP}y\sin(\alpha)\right]$$
$$\exp(ik_{SPP}x)\exp(-i\omega t - k_z z)\hat{a}_\pm, \tag{16}$$

where,

$$F(x) = \sqrt{\frac{\pi}{\left(\frac{1}{\omega_0^2} - i\frac{k_{SPP}}{2x}\right)x}} \exp\left[-\frac{k_{SPP}^2 \sin^2(\alpha)}{4\left(\frac{1}{\omega_0^2} - i\frac{k_{SPP}}{2x}\right)}\right] Erfc\left[\frac{\sqrt{k_{SPP}}x(-1+i)}{2}\sin(\alpha)\right]. \quad (17)$$

Inclined-LCGB generation

When the incident angle is β according to the y-axis, the amplitude and phase distribution of the column would be in the form of $A_m = A\exp\left[-(md)^2/W_0^2\right]$ and $\varphi_m = -k_{SPP}|md|\sin(\alpha)$ $+k_{SPP}(md)\sin(\beta), m = -N \sim N$, respectively. Then the excited SPP waves can be expressed as:

$$\vec{E}_\pm(x,y,z,t) = \sum_{m=-N}^{N} A\exp\left[-(md)^2/W_0^2\right]\exp\left[-ik_{SPP}|md|\sin(\alpha) + ik_{SPP}md\sin(\beta)\right]$$

$$\frac{\cos(\theta_m' - \theta_m)}{\sqrt{|\vec{r} - \vec{r_m}|}}\exp\left(ik_{SPP}|\vec{r} - \vec{r_m}|\right)\exp\left(-i\omega t - k_z z\right)\hat{a}_\pm. \quad (18)$$

There is a little differences compared with the above-mentioned cases. In this case, the propagation direction is no longer the x-axis, so the paraxial approximation need be re-considered in a new x-axis. And the coordinate transformation between the new coordinates $(\hat{x}O\hat{y})$ and the old coordinates (xOy) can be expressed as:

$$\begin{bmatrix} x \\ y \end{bmatrix} = \begin{bmatrix} \cos(\beta) & -\sin(\beta) \\ \sin(\beta) & \cos(\beta) \end{bmatrix}\begin{bmatrix} \hat{x} \\ \hat{y} \end{bmatrix}. \quad (19)$$

And the schematic diagram is shown in Fig. 9(a). The paraxial approximation is applied on the new coordinates and the corresponding field distribution can be obtained as:

$$\vec{E}_\pm(\hat{x},\hat{y},z,t) = A\sin(\theta)F(x)\exp\left[\frac{-\hat{y}^2}{W_0^2/\cos^2(\beta)}\right]\cos\left[k_{SPP}\hat{y}\cos(\beta)\sin(\alpha)\right]\cdots$$

$$\cdots\exp\left(ik_{SPP}\hat{x}\right)\exp\left(-i\omega t - k_z z\right)\hat{a}_\pm. \quad (20)$$

Then through the coordinate transformation, the field distribution in the old coordinates (xOy) can be obtained,

$$\vec{E}_\pm(\vec{r},t) = A\sin(\theta)F\left(\cos(\beta)x + \sin(\beta)y\right)\exp\left[\frac{-(y\cos(\beta) - x\sin(\beta))^2}{W_0^2/\cos^2(\beta)}\right]\cdots$$

$$\cdots\cos\{k_{SPP}\sin(\alpha)\left[y\cos(\beta) - x\sin(\beta)\right]\cos(\beta)\}\cdots \quad (21)$$

$$\cdots\exp\{ik_{SPP}\left[\cos(\beta)x + \sin(\beta)y\right]\}\exp\left(-i\omega t - k_z z\right)\hat{a}_\pm.$$

It is worth noting that the beam waist of inclined-LCGB increases to $W_0/\cos(\beta)$. That is because when there is an angle of β between the column and the paraxial beam, the effective spatial period would decrease to $d\cos(\beta)$ and thus the corresponding diffraction fringe would be proportional to a factor of $1/\cos(\beta)$. With such phase distribution, an inclined-LCGB can be

generated with the angle of β according to the x-axis. The corresponding wavefront distribution is shown in Fig. 9(b).
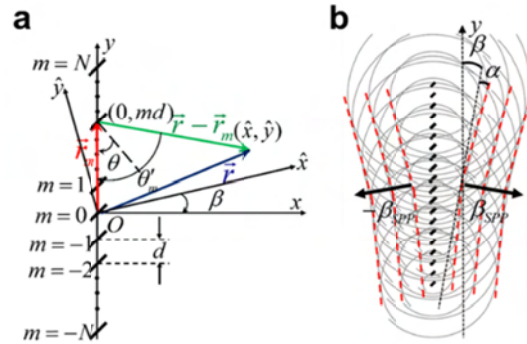
Fig. 9. (a) Top views of one column of nano-apertures with the definitions of parameters used in calculations. (b) The wavefront of an inclined-LCGB. The red dashed lines describe the shape of the wavefront and the black arrows show the propagation of generated inclined-LCGB.

The extinction conditions
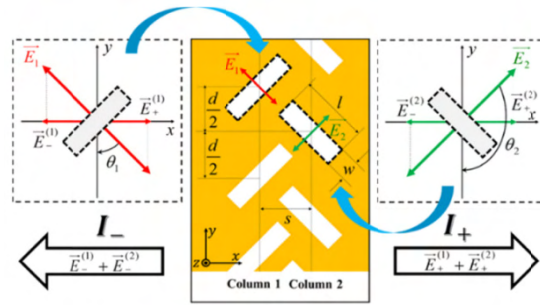
Fig. 10. Diagram of two columns of nano-slits with the definitions of parameters for generating polarization-controlled directional LCGB.

When a circularly polarized plane wave with angle frequency of ω is incident on a pair of adjacent nano-apertures in two columns as shown in Fig. 10, the time-averaged intensities of generated SPP wave in both sides can be expressed as [18]:

$$I_{\pm} \propto \left|\vec{E}_1\right|^2 \sin^2\left(\theta_1\right) + \left|\vec{E}_2\right|^2 \sin^2\left(\theta_2\right) + 2\left|\vec{E}_1\right|\left|\vec{E}_2\right|\sin\left(\theta_1\right)\sin\left(\theta_2\right)\cos\left[\left(\varphi_2 - \varphi_1\right) \mp k_{\text{SPP}} s\right], \quad (22)$$

where the subscript of i ($i = 1,2$) indicates the corresponding nano-aperture in the left or right column, $\left|\vec{E}_i\right|$ is the amplitude, θ_i is the tilt angle of nano-aperture according to the y-axis, φ_i is the initial phase of the excited SPP wave, the sign of ($\pm$) corresponds to the SPP propagating along the positive or negative x-direction, respectively. Then, the combined field of SPP along the positive and negative x-axis can be expressed as:

$$\vec{E}_{\pm}\left(x, y, z, t\right) = \left\{\left|\vec{E}_1\right|\sin\left(\theta_1\right) + \left|\vec{E}_2\right|\sin\left(\theta_2\right)\exp\left\{i\left[k_{\text{SPP}} s \pm \left(\varphi_2 - \varphi_1\right)\right]\right\}\right\}\cdots$$
$$\cdots \exp\left(\pm i k_{\text{SPP}} x\right)\exp\left(-i\omega t - k_z z\right)\hat{a}_+, \quad (23)$$

Consequently, the time-averaged intensities of SPP wave can be calculated as:

$$I_{\pm} \propto \left|\vec{E}_1\right|^2 \sin^2\left(\theta_1\right) + \left|\vec{E}_2\right|^2 \sin^2\left(\theta_2\right) + 2\left|\vec{E}_1\right|\left|\vec{E}_2\right|\sin\left(\theta_1\right)\sin\left(\theta_2\right)\cos\left[\left(\varphi_2 - \varphi_1\right) \mp k_{\text{SPP}} s\right]. \quad (24)$$

To achieve unidirectional propagation, one of the I_+ and I_- should be zero and the other one should be as large as possible. Without loss of generality, here $I_- = 0$ with $\max(I_+)$ is considered and then the following equations can be obtained.

$$\begin{cases} \left|\vec{E}_1\right|\sin(\theta_1) = \left|\vec{E}_2\right|\sin(\theta_2); \\ (\varphi_2 - \varphi_1) - k_{\text{SPP}}s = 0; \\ (\varphi_2 - \varphi_1) + k_{\text{SPP}}s = \pi. \end{cases} \tag{25}$$

For simplicity, we assume that a pair of neighboring nano-apertures in two columns have the same shape so that we have: $\left|E_1\right| = \left|E_2\right|$. The sign of $(\pm)$ in the phase term $\pm(\theta_2 - \theta_1)$ corresponds to incidence with right-handed circular polarization (RHCP)/the left-handed circular polarization (LHCP). Then the maximal extinction conditions can be obtained.

$$k_{\text{SPP}}s = \frac{\pi}{2}; \theta_1 = \frac{\pi}{4}; \theta_2 = \frac{3\pi}{4}. \tag{26}$$

The definition and measurement of extinction ratio

The extinction ratio can be expressed as:

$$\gamma = \max(T_R, T_L)\big/\min(T_R, T_L), \tag{27}$$

where $T_{R,L}$ is the transmission coefficient of SPP wave generated in the right or left side. Due to the SPP wave generated in both sides have the same Gaussian intensity distribution (the same optical waist in symmetric position of both sides), thus the extinction ratio could be approximately given by the ratio of peak intensity.

$$\gamma = \max(I_R, I_L)\big/\min(I_R, I_L), \tag{28}$$

where $I_{R,L}$ is the peak intensity of SPP wave generated in the right or left side. Figures 11(a1)-11(a3) show the intensity distribution of scattering signals of LCGB with $\alpha = 3°$ along the propagation direction across the center of the coupler (the red dashed line) for different SOP. Then the peak intensity of left and right side can be obtained. The extinction ratio can be expressed by $(I_A-I_b)/(I_B-I_b)$, $(I_D-I_b)/(I_C-I_b)$, $(I_F-I_b)/(I_E-I_b)$ for incidence with RHCP, LHCP and LP, respectively, where I_b is the intensity of background light.
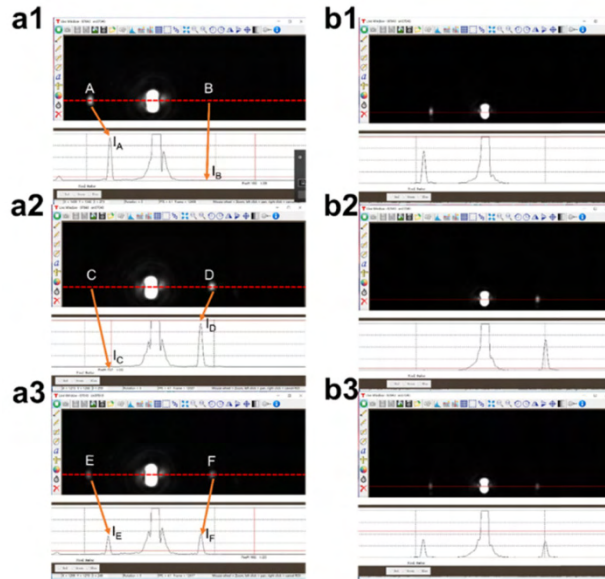
Fig. 11. (a1-a3) The experimental results of $\alpha = 3°$ for incidence with RHCP, LHCP and LP. (a1) The intensity distribution of scattering signals by gratings along the propagation direction across the center of the coupler (the red dashed line) is plotted by the CCD camera. (I_A, I_B) refer to the peak intensity of left and right side for incidence with RHCP, respectively. (a2) (I_C, I_D) refer to the peak intensity of left and right side for incidence with LHCP, respectively. (a3) (I_E, I_F) refer to the peak intensity of left side and right side for incidence with LP, respectively. (b1-b3) The corresponding experimental results for $\alpha = 5°$.

The definition and measurement of divergence angle

The beam divergence angle is defined as:

$$\theta_{div} = \lim_{x \to \infty} \frac{w(x)}{w_0},$$

(29)

where $w(x)$ is the beam width in the longitudinal position of x which is the radius of the horizontal field when the amplitude drops to $1/e$ of the maximum of optical field. Thus the key to measure the divergence angle is to measure the beam width. Firstly, the intensity distribution of the spot along the cross section can be measured. Figure 12 shows the intensity distribution along the cross section of scattering signal of LCGB with $\alpha = 3°$ in different propagation positions of 30μm, 40μm, 50μm, respectively. Then the Gaussian fitting is performed so that the half width at $1/e^2$ of maximum of the Gaussian peak can be obtained and this value is the beam width of generated SPP beam. Furthermore, the beam width is linearly fitted with longitudinal positions and the slope obtained with liner fitting would be the divergence angle.
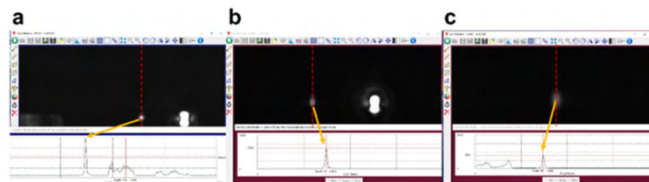
Fig. 12. (a-c) show shows the intensity distribution along the cross section of signal (red dashed line) in the propagation position of 30μm, 40μm, 50μm, respectively. The yellow arrows refer to the signal peak collected by the CCD camera.

Simulated intensity of main lobe vs. longitudinal position for LCGB with α = 3°

Figure 13 shows intensity of main lobe vs. longitudinal position for LCGB with $\alpha=3°$. It could be found that the normalized intensity is still larger than 0.5 at the position of 60μm. It means that the SPP propagation length (defined as the length while the intensity reduces to $1/e^2$) would be longer than 60μm. Therefore, in our case, the non-diffracting length (58μm) is adopted as a conservative estimation of the SPP propagation characteristics.
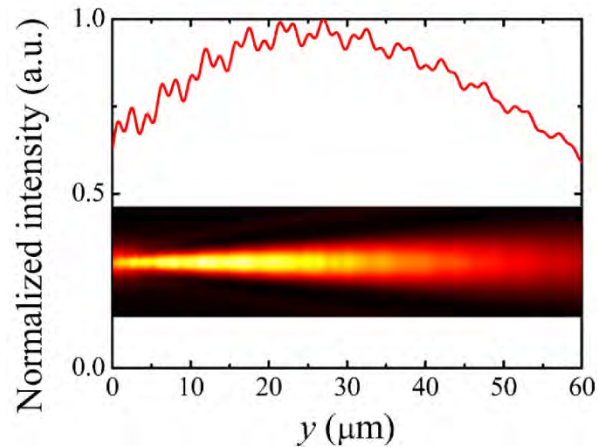
Fig. 13. Shows the relation between intensity of main lobe and longitudinal position for LCGB with $\alpha = 3°$ generated by the proposed device. The field distribution is also given in the inset.

Experimental results for LCGB with α = 5°

Figure 14(a) is the scanning electron microscope (SEM) image of the whole structure composed of LCGB couplers with $\alpha=5°$ and the enlarged area shows the details. There are five couplers aligned together to form a coupler group with a period of one SPP wavelength (~0.96μm) to achieve higher excitation efficiency. Besides, there are two annular gratings in both sides to scatter the generated LCGB into propagating mode in free-space for measurement and the distance between the two gratings is about 65μm. Figure 14(b) shows the optical field collected by the CCD camera when the polarization-controlled LCGB directional generators with $\alpha=5°$ are illuminated by light with different SOP. Figure 14(c) shows the optical field collected by the CCD camera for incidence with LHCP in different longitudinal positions (30μm, 40μm, 50μm).
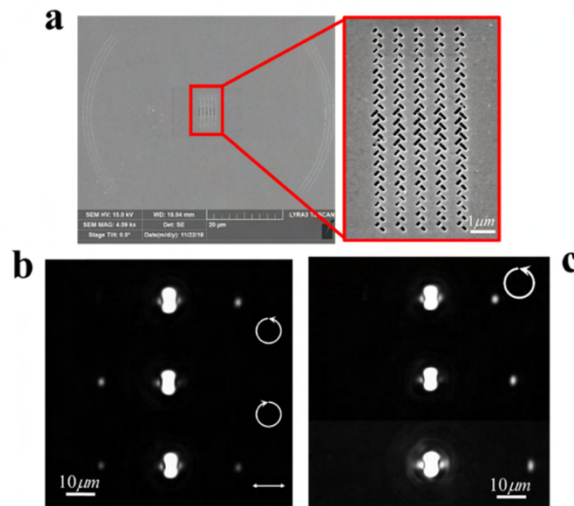
Fig. 14. Experimental results for polarization controlled directional LCGB generator with $\alpha =$ 5°. (a) The SEM image of the whole structure and the annular gratings in both sides to scatter the generated LCGB into propagating mode in free-space for measurement. The enlarged area shows the couplers group composed of five polarization-controlled directional LCGB couplers with $\alpha =$ 5°. (b) The scattering signals of polarization-controlled directional propagation of generated LCGB for incidence with LHCP, RHCP and LP, respectively. (c) The experimental results for incidence with LHCP in different longitudinal positions (30μm, 40μm, 50μm).

Funding

Acknowledgment

References

1. W. L. Barnes, A. Dereux, and T. W. Ebbesen, "Surface plasmon subwavelength optics," Nature **424**(6950), 824–830 (2003).
2. A. I. Fernández-Domínguez, F. J. García-Vidal, and L. Martín-Moreno, "Unrelenting plasmons," Nat. Photonics **11**(1), 8–10 (2017).
3. E. Ozbay, "Plasmonics: Merging Photonics and Electronics At Nanoscale Dimensions," Science **311**(5758), 189–193 (2006).
4. R. Zhang, Y. Zhang, Z. C. Dong, S. Jiang, C. Zhang, L. G. Chen, L. Zhang, Y. Liao, J. Aizpurua, Y. Luo, J. L. Yang, and J. G. Hou, "Chemical mapping of a single molecule by plasmon-enhanced Raman scattering," Nature **498**(7452), 82–86 (2013).
5. M. Kauranen and A. V. Zayats, "Nonlinear plasmonics," Nat. Photonics **6**(11), 737–748 (2012).
6. M. Mesch, B. Metzger, M. Hentschel, and H. Giessen, "Nonlinear Plasmonic Sensing," Nano Lett. **16**(5), 3155–3159 (2016).
7. K. Wang, E. Schonbrun, P. Steinvurzel, and K. B. Crozier, "Trapping and rotating nanoparticles using a plasmonic nano-tweezer with an integrated heat sink," Nat. Commun. **2**(1), 469 (2011).
8. C. Min, Z. Shen, J. Shen, Y. Zhang, H. Fang, G. Yuan, L. Du, S. Zhu, T. Lei, and X. Yuan, "Focused plasmonic trapping of metallic particles," Nat. Commun. **4**(1), 2891 (2013).
9. P. P. Patra, R. Chikkaraddy, R. P. N. Tripathi, A. Dasgupta, and G. V. P. Kumar, "Plasmofluidic single-molecule surface-enhanced Raman scattering from dynamic assembly of plasmonic nanoparticles," Nat. Commun. **5**(1), 4357 (2014).
10. D. K. Gramotnev and S. I. Bozhevolnyi, "Plasmonics beyond the diffraction limit," Nat. Photonics **4**(2), 83–91 (2010).
11. W. F. Andress, H. Yoon, K. Y. M. Yeung, L. Qin, K. West, L. Pfeiffer, and D. Ham, "Ultra-Subwavelength Two-Dimensional Plasmonic Circuits," Nano Lett. **12**(5), 2272–2277 (2012).

12. R. W. Heeres, L. P. Kouwenhoven, and V. Zwiller, "Quantum interference in plasmonic circuits," Nat. Nanotechnol. **8**(10), 719–722 (2013).
13. M. Ayata, Y. Fedoryshyn, W. Heni, B. Baeuerle, A. Josten, M. Zahner, U. Koch, Y. Salamin, C. Hoessbacher, C. Haffner, D. L. Elder, L. R. Dalton, and J. Leuthold, "High-speed plasmonic modulator in a single metal layer," Science **358**(6363), 630–632 (2017).
14. C. Haffner, D. Chelladurai, Y. Fedoryshyn, A. Josten, B. Baeuerle, W. Heni, T. Watanabe, T. Cui, B. Cheng, S. Saha, D. L. Elder, L. R. Dalton, A. Boltasseva, V. M. Shalaev, N. Kinsey, and J. Leuthold, "Low-loss plasmon-assisted electro-optic modulator," Nature **556**(7702), 483–486 (2018).
15. R. Ritchie, E. Arakawa, J. Cowan, and R. Hamm, "Surface-Plasmon Resonance Effect in Grating Diffraction," Phys. Rev. Lett. **21**(22), 1530–1533 (1968).
16. P. Lalanne, J. P. Hugonin, and J. C. Rodier, "Approximate model for surface-plasmon generation at slit apertures," J. Opt. Soc. Am. A **23**(7), 1608–1615 (2006).
17. A. Otto, ""Excitation of nonradiative surface plasma waves in silver by the method of frustrated total reflection," Z. Für Phys.," Hadrons Nucl. **216**(4), 398–410 (1968).
18. J. Lin, J. P. B. Mueller, Q. Wang, G. Yuan, N. Antoniou, X.-C. Yuan, and F. Capasso, "Polarization-Controlled Tunable Directional Coupling of Surface Plasmon Polaritons," Science **340**(6130), 331–334 (2013).
19. L. Zhu, Y. Li, A. Sun, Z. Xiong, C. Liu, Y. Kong, and S. Wang, "Active-polarization-controlled long-depth focus generated by orthogonal nanoslit array," Appl. Phys. Express **9**(8), 082201 (2016).
20. J. Lin, J. Dellinger, P. Genevet, B. Cluzel, F. de Fornel, and F. Capasso, "Cosine-Gauss Plasmon Beam: A Localized Long-Range Nondiffracting Surface Wave," Phys. Rev. Lett. **109**(9), 093904 (2012).
21. K. Xiao, S. Wei, C. Min, G. Yuan, S. W. Zhu, T. Lei, and X.-C. Yuan, "Dynamic cosine-Gauss plasmonic beam through phase control," Opt. Express **22**(11), 13541–13546 (2014).
22. P. Qiu, D. Zhang, M. Jing, T. Lu, B. Yu, Q. Zhan, and S. Zhuang, "Dynamic tailoring of surface plasmon polaritons through incident angle modulation," Opt. Express **26**(8), 9772–9783 (2018).
23. X. He, T. Ning, R. Li, L. Pei, J. Zheng, and J. Li, "Dynamical manipulation of Cosine-Gauss beams in a graphene plasmonic waveguide," Opt. Express **25**(12), 13923–13932 (2017).
24. I. Epstein, R. Remez, Y. Tsur, and A. Arie, "Generation of intensity-controlled two-dimensional shape-preserving beams in plasmonic lossy media," Optica **3**(1), 15 (2016).
25. P. Qiu, T. Lv, Y. Zhang, B. Yu, J. Lian, M. Jing, and D. Zhang, "Polarization Controllable Device for Simultaneous Generation of Surface Plasmon Polariton Bessel-Like Beams and Bottle Beams," Nanomaterials (Basel) **8**(12), 975 (2018).
26. E. Gazzola, G. Ruffato, and F. Romanato, "Propagation of grating-coupled surface plasmon polaritons and cosine–Gauss beam generation," J. Opt. Soc. Am. B **32**(8), 1564 (2015).
27. I. Epstein, Y. Lilach, and A. Arie, "Shaping plasmonic light beams with near-field plasmonic holograms," J. Opt. Soc. Am. B **31**(7), 1642 (2014).
28. D. Bar-Lev, A. Arie, J. Scheuer, and I. Epstein, "Efficient excitation and control of arbitrary surface plasmon polariton beams using one-dimensional metallic gratings," J. Opt. Soc. Am. B **32**(5), 923 (2015).
29. A. E. Minovich, A. E. Klein, D. N. Neshev, T. Pertsch, Y. S. Kivshar, and D. N. Christodoulides, "Airy plasmons: non-diffracting optical surface waves: Airy plasmons," Laser Photonics Rev. **8**(2), 221–232 (2014).
30. R. Schley, I. Kaminer, E. Greenfield, R. Bekenstein, Y. Lumer, and M. Segev, "Loss-proof self-accelerating beams and their use in non-paraxial manipulation of particles' trajectories," Nat. Commun. **5**(1), 5189 (2014).
31. O. Avayu, I. Epstein, E. Eizner, and T. Ellenbogen, "Polarization controlled coupling and shaping of surface plasmon polaritons by nanoantenna arrays," Opt. Lett. **40**(7), 1520–1523 (2015).
32. X. Yin, L. Chen, and X. Li, "Polarization-controlled generation of Airy plasmons," Opt. Express **26**(18), 23251–23264 (2018).
33. A. Minovich, A. E. Klein, N. Janunts, T. Pertsch, D. N. Neshev, and Y. S. Kivshar, "Generation and Near-Field Imaging of Airy Surface Plasmons," Phys. Rev. Lett. **107**(11), 116802 (2011).
34. I. Epstein and A. Arie, "Dynamic generation of plasmonic bottle-beams with controlled shape," Opt. Lett. **39**(11), 3165–3168 (2014).
35. P. Genevet, J. Dellinger, R. Blanchard, A. She, M. Petit, B. Cluzel, M. A. Kats, F. de Fornel, and F. Capasso, "Generation of two-dimensional plasmonic bottle beams," Opt. Express **21**(8), 10295–10300 (2013).
36. I. Epstein and A. Arie, "Arbitrary Bending Plasmonic Light Waves," Phys. Rev. Lett. **112**(2), 023903 (2014).
37. F. Ding, R. Deshpande, and S. I. Bozhevolnyi, "Bifunctional gap-plasmon metasurfaces for visible light: polarization-controlled unidirectional surface plasmon excitation and beam steering at normal incidence," Light Sci. Appl. **7**(4), 17178 (2018).
38. E.-Y. Song, S.-Y. Lee, J. Hong, K. Lee, Y. Lee, G.-Y. Lee, H. Kim, and B. Lee, "A double-lined metasurface for plasmonic complex-field generation: A double-lined metasurface for plasmonic complex-field," Laser Photonics Rev. **10**(2), 299–306 (2016).
39. L. Huang, X. Chen, B. Bai, Q. Tan, G. Jin, T. Zentgraf, and S. Zhang, "Helicity dependent directional surface plasmon polariton excitation using a metasurface with interfacial phase discontinuity," Light Sci. Appl. **2**(3), e70 (2013).
40. S.-Y. Lee, K. Kim, S.-J. Kim, H. Park, K.-Y. Kim, and B. Lee, "Plasmonic meta-slit: shaping and controlling near-field focus," Optica **2**(1), 6 (2015).
41. Q. Jiang, A. Pham, M. Berthel, S. Huant, J. Bellessa, C. Genet, and A. Drezet, "Directional and Singular Surface Plasmon Generation in Chiral and Achiral Nanostructures Demonstrated by Leakage Radiation Microscopy,"

ACS Photonics **3**(6), 1116–1124 (2016).

42. W. Tsai, Q. Sun, G. Hu, P. C. Wu, R. J. Lin, C. Qiu, K. Ueno, H. Misawa, and D. P. Tsai, "Twisted Surface Plasmons with Spin-Controlled Gold Surfaces," Adv. Opt. Mater. **7**(8), 1801060 (2019).

43. T. Tanemura, K. C. Balram, D.-S. Ly-Gagnon, P. Wahl, J. S. White, M. L. Brongersma, and D. A. B. Miller, "Multiple-Wavelength Focusing of Surface Plasmons with a Nonperiodic Nanoslit Coupler," Nano Lett. **11**(7), 2693–2698 (2011).